



OPEN Investigation of the effect of crystal size on the piezoelectric features of lead-free barium titanate ceramic using molecular dynamics simulation

S. Esmaeili¹, M. H. Ehsani¹✉, Davood Toghraie² & S. Saber-Samandari³

This study investigated the piezoelectric properties of BaTiO₃ ceramics with different sizes through molecular dynamics simulations. The results show that all samples reached thermal equilibrium at 300 K and equilibrium in potential energy within 10 ns, confirming effective equilibration. As the size of the ceramics increased, the mean square displacement and diffusion coefficients decreased from 0.217 and 0.0034 to 0.1934 Å² and 0.003 Å²/ns, attributed to a more uniform microstructure with fewer defects, resulting in reduced ion mobility. Furthermore, saturation polarization, residual polarization, and coercive field values increased from 0.35, 0.1, and 0.175 to 0.42 C/m², 0.16 C/m², and 0.282 MV/m, respectively, with increasing sample size, highlighting enhanced polarization responses due to a greater volume of ferroelectric material. Larger barium titanate (BaTiO₃) crystals can have better polarization due to more domains aligning, but they may not deform as much (lower strain) because the walls among those domains can't move freely. While improved domain alignment contributed to higher polarization, the increased stress can restrict the mobility of the domain walls. These findings provided valuable insights into the size-dependent behavior of BaTiO₃ ceramics, essential for optimizing their applications in electronic devices and sensors. The study underscored the importance of understanding microstructural effects on material properties for future advancements in ferroelectric technology.

Keywords Crystal size, Piezoelectric features, Lead-free barium titanate, Molecular dynamics simulation

Lead-free BaTiO₃ ceramics are increasingly significant in the field of materials science due to their excellent piezoelectric properties and environmental benefits^{1,2}. As industries move away from lead-based materials due to health and environmental concerns, lead-free alternatives like BaTiO₃ are becoming essential³. These ceramics maintain high performance in applications such as sensors, actuators, and capacitors, making them suitable for various electronic devices^{4–6}. Their ability to convert mechanical energy into electrical energy and vice versa is crucial for the development of sustainable technologies. The importance of BaTiO₃ ceramics extends beyond their functional capabilities; they also align with global initiatives aimed at reducing hazardous materials in manufacturing. By providing a safer alternative, these ceramics contribute to greener production processes and the creation of eco-friendly products. Their adoption can lead to innovations in energy harvesting, medical devices, and consumer electronics, ultimately fostering advancements in technology while prioritizing environmental responsibility^{7–9}. Investigating the effect of crystal size on the piezoelectric features of BaTiO₃ ceramics is crucial for several reasons. The term 'crystal size' specifically refers to the dimensions of the ordered crystalline regions within the BaTiO₃ structure, where these dimensions significantly increase in one direction. These crystalline regions are characterized by their well-defined atomic arrangements and contribute significantly to the material's properties, including its piezoelectric behavior. In contrast, 'grain size' pertains to the overall dimensions of the grains within a polycrystalline ceramic matrix. Each grain consists of numerous crystallites oriented differently and separated by grain boundaries. Crystal size can significantly affect microstructure, which in turn affects electrical and mechanical properties. Larger crystal sizes may enhance the piezoelectric response due to the

¹Faculty of Physics, Semnan University, P.O. Box, Semnan 35195-363, Iran. ²Department of Mechanical Engineering, Khomeinishahr Branch, Islamic Azad University, Khomeinishahr, Iran. ³New Technologies Research Center, Amirkabir University of Technology, Tehran, Iran. ✉email: Ehsani@semnan.ac.ir

decreased surface-to-volume ratio and a more uniform distribution of stress across the crystal, leading to better performance in applications such as sensors and actuators¹⁰. Understanding how crystal size affect piezoelectric features can guide the optimization of manufacturing processes. By controlling crystal growth, researchers can tailor the piezoelectric properties of BaTiO₃ ceramics to meet specific application requirements.

Wang et al.¹¹ focused the dispersion of BaTiO₃ nanoparticles in polyvinylidene difluoride (PVDF) to enhance the piezoelectric properties of wearable nanogenerators. The study demonstrated that core-shell structured F@BT nanoparticles significantly improved both dispersion and performance, achieving an output voltage of 2.1 V and stable operation over 1000 cycles for applications in motion sensing and energy harvesting. Cai et al.¹² focused how atomic vacancies in perovskite-type BT ceramics significantly affected their crystal structure and electrical properties, leading to lattice deformation and preferred orientations. The study revealed that these vacancies resulted in low resistance, increased leakage currents, and reduced breakdown strength, while also affecting mechanical properties and decreasing the piezoelectric constant along with z-axis. Chen et al.¹³ examined the effects of Sr-doping on BT-based ceramics. The results demonstrate that carefully controlled doping can enhance piezoelectric performance, while excessive Sr-doping led to a deterioration in piezoelectric properties. In our previous work¹⁴, we used molecular dynamics (MD) simulations to explore how temperature (Temp) affected the piezoelectric properties of tetragonal BT crystals. As Temp increased from 300 to 400 K, the diffusion coefficient increased, while the piezoelectric coefficient, saturation polarization, coercivity, and residual polarization decreased, indicating structural changes from tetragonal to cubic near the critical Temp.

The effect of crystal size on the piezoelectric features of lead-free BaTiO₃ ceramics was investigated using MD simulations. These simulations allowed for a detailed understanding of how variations in crystal size affected the material's microstructure and, consequently, its piezoelectric properties. By simulating atomic interactions and movements at different scales, researchers can observe how changes in crystal size affect domain switching, polarization, and overall piezoelectric performance¹⁵. This knowledge is crucial for optimizing material properties for specific applications. The advantages of using MD simulation included the ability to model complex systems at the atomic level, providing insights that are difficult to obtain through experimental methods alone^{16,17}. Additionally, these simulations can help predict material behavior over time, allowing for the identification of optimal crystal sizes that enhance piezoelectric properties. For this purpose, stress-strain curve, mean square displacement (MSD), diffusion coefficient, strain-electric field (S-E) relationship, hysteresis loop (butterfly loop), and polarization-electric field (P-E) hysteresis loops (ferroelectric loop) at different sizes of BaTiO₃ ceramics are investigated. The results of this study ultimately helped in the design and development of more efficient and effective lead-free piezoelectric materials for various technological applications.

Molecular dynamics simulation

Present simulation details

The effect of crystal size on the piezoelectric features of BaTiO₃ ceramic was analyzed through MD simulations. The initial phase involved constructing a structural model using Avogadro software¹⁸, with the simulation box dimensions of 80 × 40 × 40 Å³ (Sample A), 80 × 80 × 40 Å³ (Sample B), and 80 × 80 × 80 Å³ (Sample C) across all axes (See Fig. 1). Periodic boundary conditions were applied in all 3 directions to ensure a continuous simulation environment. Following the model creation, the simulation proceeded in two distinct phases. The first phase focused achieving equilibrium within the simulated structure using the constant number of particles (N), volume (V), and Temp (T) ensemble (NVT or canonical ensemble). The initial Temp was maintained at 300 K. To regulate the Temp, the Nose-Hoover thermostat was employed, allowing for precise control. Changes in the kinetic and total potential for 10 ns were monitored to assess the equilibration of the initial structures. Once equilibrium was established, the simulation transitioned to the constant number of particles (N), volume (V), and energy (E) ensemble (NVE or microcanonical ensemble). This change enabled the examination of the piezoelectric properties of structures. By analyzing the effects of crystal size, insights into the relationship between atomic structure and piezoelectric performance were gained. The initial configurations of the structures were visually represented in a schematic diagram, providing a clear illustration of the model used in the simulations.

Equilibration process

The equilibration process in MD simulations is crucial for ensuring that the system reached a stable state before any meaningful analysis can be conducted. During equilibration, the initial configuration of model was allowed to relax, which helped minimize energy and establish appropriate atomic positions and velocities. This step was essential because it ensured that the system was not in a highly strained or unrealistic configuration, which could lead to erroneous results in subsequent simulations. Proper equilibration allowed for more accurate predictions of material properties and behaviors. Temp control during the equilibration phase was particularly important, as it affected the dynamics of particles within the simulation. Using methods, such as the Nose-Hoover thermostat helped maintain a constant Temp, allowing researchers to observe how the system responded to thermal fluctuations. Temp change curve generated during this process provided valuable insights into the system's thermal stability and response to energy input. A well-defined Temp profile indicates that the system has reached equilibrium, while large fluctuations may suggest that further equilibration is needed. Figure 2 reveals the changes in the Temp of samples A, B, and C. The results shown in Fig. 2 demonstrate the convergence of Temp to 300 K after 10 ns in all samples. This convergence indicated that the system successfully reached thermal equilibrium. This stability suggested that the initial conditions set during the equilibration phase were effective in allowing the particles to adjust to their surroundings. A consistent Temp across different samples implied that the MD simulation accurately reflected realistic thermal behavior, which was essential for reliable results in further analyses.

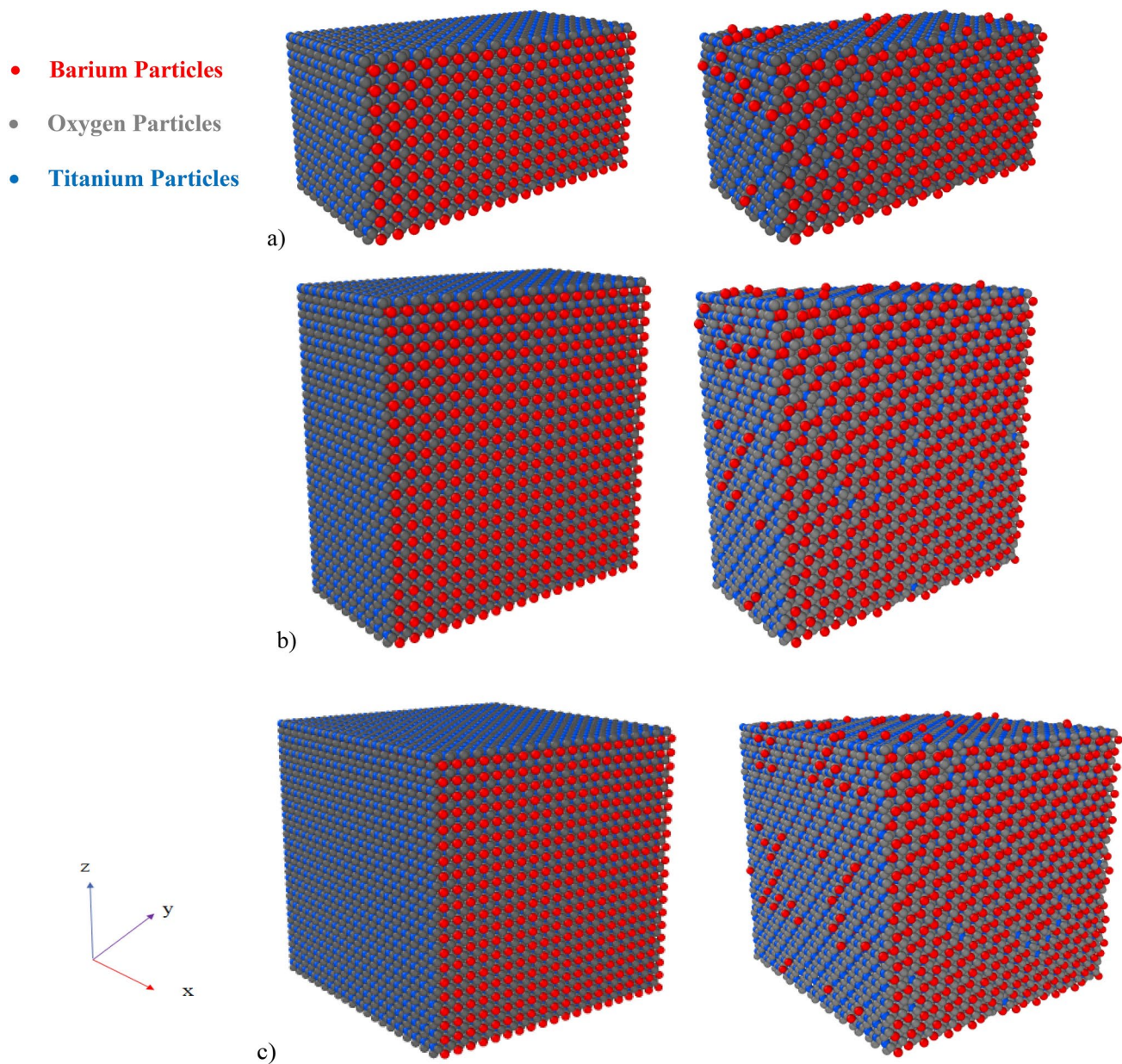


Fig.1. A perspective view of simulated BaTiO₃ ceramic of (a) A, (b) B, and (c) C samples in the first and last time steps.

Figure 3 reveals the changes in the potential energy of samples A, B, and C during 10 ns. In MD simulations, the potential energy was calculated based on the interactions between atoms or molecules within a system. This included the contributions from various forces, such as van der Waals forces, electrostatic interactions, and covalent bonds. The potential energy U can be computed using force fields that describe how particles interact. The results reveal that the potential energy of samples converged to $-30,858.744$, $-61,715.374$, and $-123,431.51$ eV, respectively. For a system to be considered in thermodynamic equilibrium, the potential energy must converge to a stable value. This indicated that the system explored its configurational space adequately and was no longer affected by transient states or artifacts from initial conditions. The properties derived from MD simulations, such as structural, dynamical, and thermodynamic characteristics, rely heavily on the convergence of potential energy. If the potential energy did not converge, the calculated properties may not reflect true equilibrium values, leading to erroneous interpretations of molecular behavior. On the other hand, the negative potential energy values suggested that the crystal structure was stable and energetically favorable. Systems naturally evolved towards configurations that minimized their potential energy, leading to more stable arrangements of atoms or molecules within the crystal lattice. Therefore, convergence indicated that the atoms or molecules were held together by attractive forces, resulting in a stable arrangement that minimizes energy. In larger crystals, the reduction of surface effects and the ability to accommodate defects lead to configurations that were energetically favorable, allowing the system to reach lower potential energy levels. Consequently,

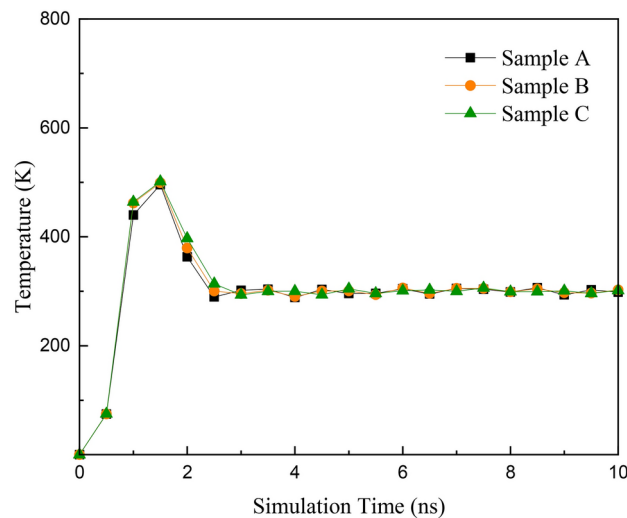


Fig. 2. The changes in Temp of samples A, B, and C.

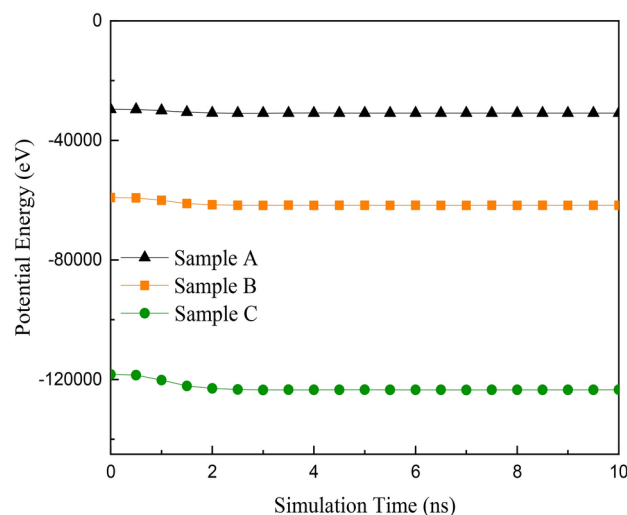


Fig. 3. The changes in potential energy of samples A, B, and C.

this stability reflected a thermodynamically favorable condition where the likelihood of phase transitions or structural changes was minimized, enhancing the reliability of simulation results. Larger crystals converging towards more negative potential energy indicated that they were more tightly bound, and less likely to undergo phase transitions or structural changes under normal conditions.

Validation

Investigating the stress–strain curve was crucial for validating the mechanical properties of ceramic materials. This curve provided insights into how the material deformed under applied stress. A well-defined stress–strain curve indicated that the material behaved predictably under load, which was essential for applications requiring structural integrity. By analyzing these curves, researchers can confirm that the simulated properties aligned with experimental data, thereby validating the accuracy of MD simulations and the effectiveness of chosen force fields. Figure 4 represents the ferroelectric stress–strain curves for samples A, B, and C. The obtained ferroelectric stress–strain curve were in good agreement with Lematre et al.¹⁹, which showed the validation of the present studies (Fig. 4b). As shown in Fig. 4, there was a linear relationship between stress and strain at lower stress levels, indicating elastic behavior. As the applied force increased, the relationship deviated from linearity, leading the material into the plastic deformation region, where deformation became permanent and irreversible. In this phase, sufficient stress caused ferroelectric domains to shift direction, aligning perpendicular to the applied force. The results obtained in this part indicate that by increasing the size of the ceramic material, the stress magnitude increased, as observed consistently across samples A, B, and C. As the size of ceramic increased, the material's structural integrity improved, leading to greater resistance against deformation. Larger

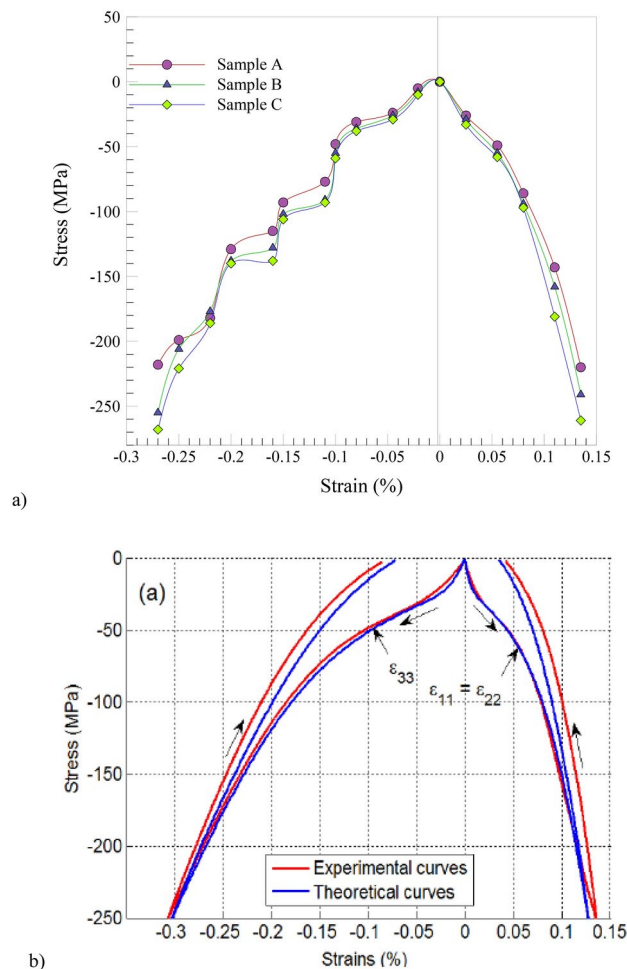


Fig. 4. The stress–strain curve of (a) all present samples and (b) Lematre et al.¹⁹.

crystals exhibited enhanced interatomic interactions and reduced surface effects, which means that more force was required to cause plastic deformation. This resulted in a higher yield strength, meaning that a greater applied stress was necessary to initiate the transition from elastic to plastic behavior. Additionally, the alignment of ferroelectric domains became more pronounced in larger samples, contributing to increased stress thresholds before irreversible deformation occurs. Consequently, the combination of these factors led to a consistent increase in stress magnitude across samples A, B, and C, as their size increased.

Results and discussion

In this section, the change in MSD, diffusion coefficient, strain–electric field (S–E) hysteresis loop (butterfly loop), and polarization–electric field (P–E) hysteresis loops (ferroelectric loop) at different sizes of BaTiO₃ ceramics were investigated. MSD is a statistical measure used to quantify the average squared distance particles moved from their initial positions over time. It provided insights into the dynamics of particle motion in various systems. By calculating the MSD, researchers can understand how particles diffuse and explore the underlying mechanisms driving their movement. MSD is particularly useful in characterizing diffusive behavior, as it relates directly to the random walk model, where particles undergo a series of random steps. The MSD is represented as following²⁰:

$$MSD = \langle r_i^2(t) \rangle = \frac{1}{N} \sum_{i=1}^N [r_i(t) - r_i(0)]^2. \quad (1)$$

The diffusion coefficient is a crucial parameter that describes how quickly particles spread through a medium. It can be derived from MSD by analyzing the relationship between the MSD and time. For a system undergoing normal diffusion, the MSD increases linearly with time, and the diffusion coefficient is represented as follows²¹:

$$MSD = 6Dt + \text{constant}. \quad (2)$$

Figure 5 represent the MSD of different samples. The results reveal that with increasing size of the ceramic, MSD and diffusion coefficient decreased. Numerical results are listed in Table 1. Larger crystals had a lower surface-to-

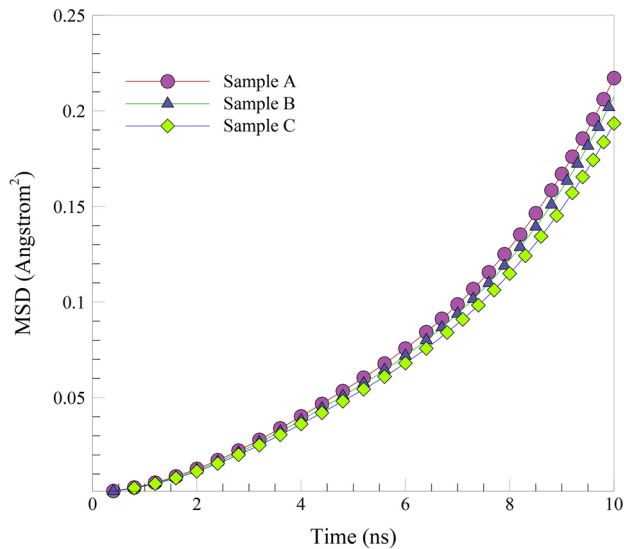


Fig. 5. The MSD curve of all samples with different sizes.

| Sample | MSD (Å²) | Diffusion coefficient (Å²/ns) | Saturation polarization (C/m²) | Residual polarization (C/m²) |
|--------|----------|-------------------------------|--------------------------------|------------------------------|
| A | 0.21719 | 0.0034 | 0.35 | 0.1 |
| B | 0.20735 | 0.0032 | 0.38 | 0.12 |
| C | 0.19345 | 0.0030 | 0.42 | 0.16 |

Table 1. The change in MSD, diffusion coefficient, of samples with different sizes.

volume ratio, which minimized the effect of surface defects and irregularities that can lead to increased atomic mobility. This resulted in more stable lattice structures, reducing the overall displacement of atoms. Additionally, as crystal size increased, the structural integrity improved, resulting in more rigid frameworks. This rigidity restricted atomic movement, thereby decreasing the MSD. In larger crystals, atoms experienced stronger cohesive forces due to more extensive interatomic interactions within the bulk material. These forces effectively limited the range of motion for individual atoms, contributing to decreased MSD values. Additionally, in larger BaTiO₃ ceramics, the interactions among ferroelectric domains can become more complex. The alignment and switching of these domains, which were crucial for the material's dielectric properties, may be hindered by the larger size, further reducing ion mobility and contributing to lower diffusion rates.

The polarization–electric field (P–E) hysteresis loop, often referred to as the ferroelectric loop, was a graphical representation that illustrated the relationship between the electric polarization of a ferroelectric material and the applied electric field. This loop was crucial for understanding the ferroelectric properties of materials like BaTiO₃. In a typical P–E hysteresis loop, the x-axis represented the applied electric field (E), while the y-axis showed the induced polarization (P) of the material. As the electric field increased, the polarization initially increased, reaching a point of saturation where further increases in the field did not result in significant changes in polarization. When the field reversed, the polarization also reversed, but this switching did not occur instantaneously, leading to a loop shape. The area enclosed by the loop represents energy loss during polarization and depolarization cycles, which was important for applications in capacitors and memory devices. The polarization is computed using equation²²:

$$P = \sum_i q_i \cdot r_i. \tag{3}$$

In above Eq., q_i is the charge of particle i and r_i is its displacement. The electric field E is applied, and the resulting polarization P is measured. Key features of the P–E hysteresis loop included saturation polarization (the maximum polarization reached), residual polarization (the polarization remaining when the electric field is removed), and coercive field (the field strength required to reduce the polarization to zero). These parameters provided insights into the efficiency and performance of ferroelectric materials in various applications, such as sensors, actuators, and non-volatile memory. The results reveal that with increasing size, saturation polarization and residual polarization increased (see Fig. 6). The numerical results are reported in Table 1. The larger BaTiO₃ samples generally contained a greater volume of ferroelectric material, enhancing the overall polarization response when an electric field was applied. The increased number of ferroelectric domains allowed for more significant alignment under an external electric field, leading to higher saturation polarization values. This larger volume can also lead to more effective domain wall movement, contributing to a more substantial residual

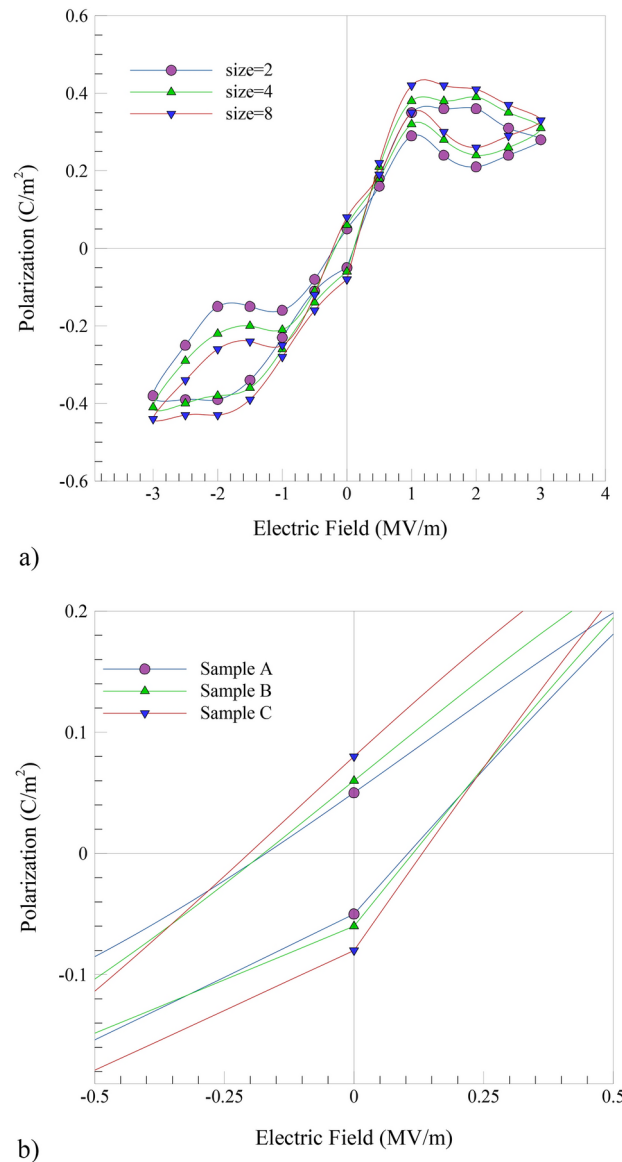


Fig. 6. The (a) P-E diagram of all samples and (b) the magnified off hysteresis loop.

polarization after the electric field was removed. Additionally, in larger samples, the domain walls may face increased resistance to movement because of mechanical constraints and interactions between neighboring domains. This can lead to a higher coercive field, as a stronger electric field was required to overcome these obstacles and switch the polarization. S. L. Miller et al.²³ emphasized domain switching as the key mechanism in the P-E loop, describing how the alignment of ferroelectric domains under an external electric field contributed to hysteresis behavior. This model provided a detailed explanation of how polarization changed with applied electric fields due to the reorientation of domains. Also, J. Yu et al.²⁴ derived a compact model for the description of the P-E hysteresis behavior based on dipole switching theory. Simulation results showed good agreement with experiments for various hysteresis loops, and the mathematical description can be easily integrated with electronic design automation software for circuit simulation. Therefore, the model can be used for circuit simulation and enhancing understanding of ferroelectric material behavior.

The strain-electric field (S-E) hysteresis loop, commonly known as the butterfly loop, represents the relationship between the mechanical strain of a material and the applied electric field (see Fig. 7). Strain is typically calculated as:

$$\varepsilon = \frac{\Delta L}{L_0}, \quad (4)$$

where ΔL is the change in length and L_0 is the initial length of the material. The electric field can be applied in LAMMPS, and the resulting strain was calculated by measuring changes in the system's dimensions²⁵.

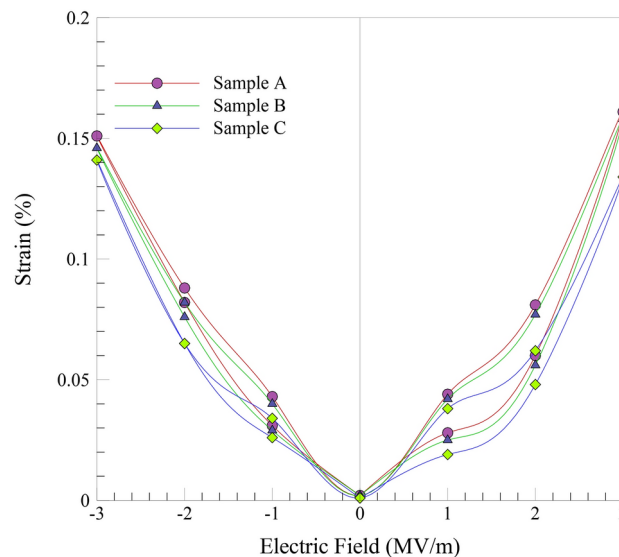


Fig. 7. The S-E diagram of all samples.

In this loop, the x-axis denotes the applied electric field (E), while the y-axis indicates the induced strain (S). As the electric field increased, the strain initially increased until it reached saturation. When the field reversed, the strain decreased, but did not return to its original state immediately, resulting in the characteristic butterfly shape of the loop. This behavior illustrated the nonlinear response of ferroelectric materials to electric fields. The S-E hysteresis loop provided valuable insights into the electromechanical coupling in ferroelectric and piezoelectric materials, revealing how they converted electrical energy into mechanical energy and vice versa. Diagrams of the S-E loop in a bipolar state are shown in Fig. 7. The butterfly diagram showed that the maximum strain decreased with increasing sample size. In larger samples, the increased volume can lead to more complex interactions among ferroelectric domains, which may hinder the ease of domain wall movement. This can result in a reduced strain response for a given electric field, leading to a smaller effective loop area. The Landau Free Energy Model focused phase transitions and the stability of different phases in ferroelectric materials. It described the free energy landscape that governed the polarization states of ferroelectric materials and explained how the energy barriers between these states led to the characteristic hysteresis in both P-E and S-E loops²⁶. Y.L. Wang et al.²⁷ into our discussion to strengthen the explanation of size effects on ferroelectric behavior. In their work, Wang et al. studied the size effect on ferroelectricity in epitaxial $\text{SrRuO}_3/\text{BaTiO}_3/\text{SrRuO}_3$ capacitors. They modified the mean-field Landau-type theory to account for dipole-dipole interaction energy, realistic lattice structure, epitaxial stress, and metal electrodes. Their results demonstrated that reducing the lateral dimensions of the film enhances spontaneous polarization, a finding that was highly relevant to our study.

Figure 8 shows the changes in the polarization-strain graph as crystal size increases. The results indicate that as crystal size increased, the polarization coefficient of structure increased. In larger crystals, there were typically fewer grain boundaries and defects, which disrupted domain wall movement. This reduction in obstacles allowed for more efficient domain wall movement under an applied electric field, resulting in a stronger polarization response. Overall, larger crystals can accommodate more ferroelectric domains that aligned more effectively with the applied electric field. The ability of these domains to reorient and align contributed to higher overall polarization, as the volume of aligned dipoles increased. Additionally, larger crystal size provided a greater material volume for polarization effects to occur. This means that the contribution of each aligned dipole to the overall polarization was more significant in larger crystals, leading to an increase in the polarization coefficient.

Figure 9 shows the changes in the dielectric constant graph as crystal size increases. Numerical results indicate that the dielectric constant increased from 73 to 82 with increasing crystal size. The increase in the dielectric constant with larger crystal size can be attributed to the material's enhanced polarizability. In larger crystals, the number of grain boundaries and defects typically decreased, allowing for a more uniform distribution of the electric field throughout the material. This uniformity facilitated the alignment of dipoles, leading to an overall increase in the material's polarization under an applied electric field. As more dipoles align, the material can store more electrical energy, resulting in a higher dielectric constant. Additionally, the larger crystal volume allowed for greater participation of ferroelectric domains, further enhancing the material's ability to respond to external electric fields.

Figure 10 shows the changes in the dielectric loss graph as crystal size increased. Numerical results indicate that dielectric loss increased from 0.044 to 0.051 as crystal size increased. The increase in dielectric loss with larger crystal size can be explained by the enhanced mobility of charge carriers and dipoles in the larger structure. As crystal size increased, the reduction in defects and grain boundaries can result in greater ionic and electronic mobility. While this improved mobility can enhance dielectric performance, it also means that as dipoles and charge carriers moved and reoriented in response to the applied electric field, the likelihood of energy loss also increased. This energy loss manifested as an increase in dielectric loss. Therefore, while the dielectric constant

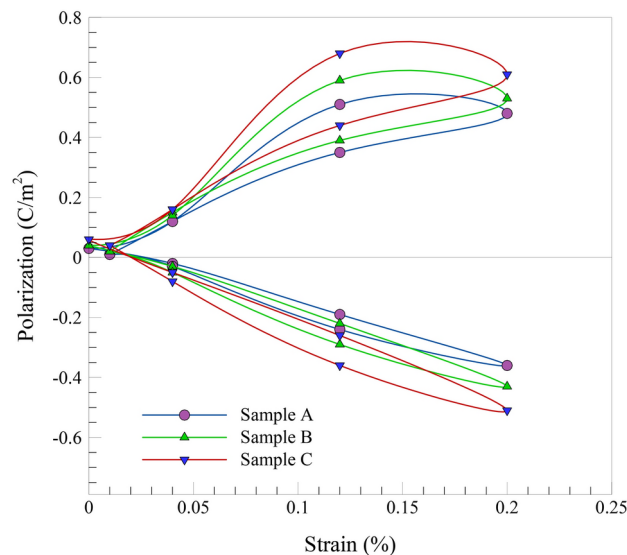


Fig. 8. Changes in the strain-polarization graph of BaTiO₃ structure as the crystal size increases.

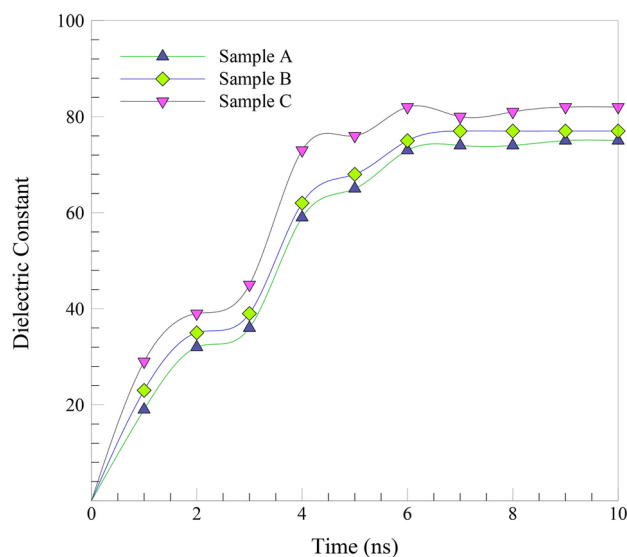


Fig. 9. Changes in the dielectric graph of BaTiO₃ structure as the crystal size increases.

increased due to improved polarization, the dielectric loss also increased due to the increased mobility and interactions of charge carriers in the larger crystal structure (Table 2).

The relationship between the microstructure of BaTiO₃ ceramics and their macroscopic properties was directly affected by changes in crystal size. As the crystal size increased, the number of grain boundaries and defects typically decreased, leading to a more uniform and organized structure. This reduction in defects allowed for more efficient domain wall movement under an applied electric field, enhancing the material's polarization response. The increased crystal size also resulted in a more homogeneous electric field distribution across the material, improving the dielectric constant. At the macroscopic level, these microstructural changes manifested as higher saturation polarization and coercive field, as well as a reduction in strain response under applied fields. The enhanced uniformity in larger crystals supported more effective alignment of dipoles, which contributed to better overall material performance, particularly in applications requiring high dielectric and ferroelectric properties. Therefore, the increase in crystal size not only improved the material's stability at the microstructural level, but also led to notable improvements in its macroscopic properties, such as dielectric constant and polarization.

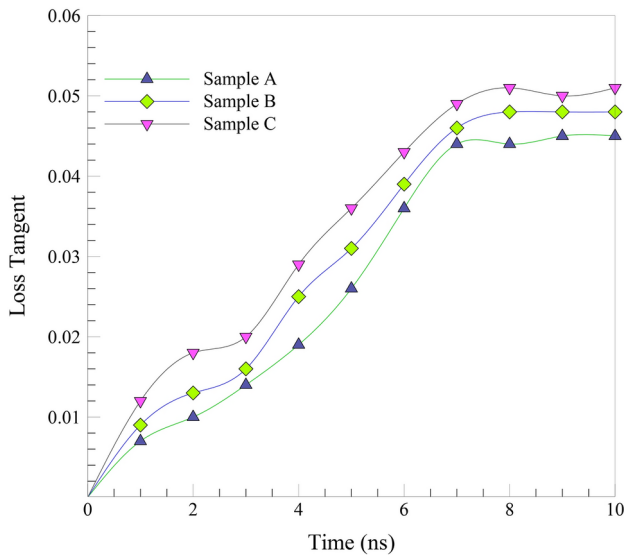


Fig. 10. Changes in the dielectric loss graph of BaTiO₃ structure as the crystal size increases.

| Sample | Piezoelectric coefficient (pC/N) | Dielectric constant | Dielectric loss |
|--------|----------------------------------|---------------------|-----------------|
| A | 208.65 | 75 | 0.045 |
| B | 245.19 | 77 | 0.045 |
| C | 285.57 | 82 | 0.082 |

Table 2. The change in piezoelectric constant, dielectric constant, and dielectric loss of samples with different sizes.

Conclusion

In summary, this study investigated the effect of crystal size on the piezoelectric features of lead-free BaTiO₃ ceramic using MD simulation. The stress–strain curve, mean square displacement (MSD), diffusion coefficient, S–E hysteresis loop, and P–E hysteresis loops across different sizes of BaTiO₃ ceramics were investigated. The results indicate that all samples (A, B, and C) successfully reached thermal equilibrium at 300 K, indicating effective initial conditions and realistic thermal behavior. The convergence of potential energy to negative values across samples signified stable structural configurations, essential for accurately predicting material properties. As the size of the BaTiO₃ ceramics increased, notable trends were observed: larger samples demonstrated enhanced stability from stronger atomic interactions, reflected in higher final stress levels, and reduced MSD and diffusion coefficients. This uniformity in microstructure minimized defects, thereby reducing ion mobility and impacting the overall diffusion process. Moreover, the results highlighted that increasing the size of ceramic led to higher saturation polarization and residual polarization, as well as an increased coercive field. The larger volume of ferroelectric material enabled more significant polarization responses, although the complexity of domain interactions in larger samples can hinder domain wall movement, resulting in reduced strain responses. Overall, these insights into the size-dependent behavior of BaTiO₃ provided a comprehensive understanding of its electromechanical properties, which was essential for optimizing its applications across various technological fields.

Data availability

The data and executable code related to this study are available upon request from the corresponding author. Please contact M. H. Ehsani at Ehsani@semnan.ac.ir for access to the data. The data will be made available in a public repository following publication.

Appendix

MD simulation

MD simulation is a powerful computational technique that allows researchers to study the behavior of atomic and molecular systems over time. Using classical mechanics principles, particularly Newton's laws of motion, MD simulations can predict how particles interact and evolve under various conditions. This approach provided insights into the microscopic mechanisms that govern material properties, enabling the exploration of phenomena that are often difficult to observe experimentally. As a result, MD simulations are invaluable in fields such as materials science, biophysics, and nanotechnology. The foundation of MD simulations relies heavily on

Newton's laws, which describe the relationship between the forces acting on a particle and its resulting motion. Specifically, the second law states that the force acting on an object is equal to the mass of that object multiplied by its acceleration. This principle enables the calculation of particle trajectories based on their initial positions and velocities. Newton's equations are represented by the following equation^{28,29}.

$$F_i = m_i a_i = -\nabla_i U = -\frac{dU}{dr_i}. \quad (\text{a-1})$$

Here, m_i denotes the particle's mass, r_i is the position vector of the particle and a_i is the acceleration. By integrating these equations over time, researchers can simulate the dynamic behavior of systems at the atomic level, yielding a detailed understanding of how materials respond to external stimuli, such as Temp changes and mechanical stress. One of the key numerical methods used in MD simulations is the Velocity-Verlet algorithm. This algorithm is particularly advantageous because it conserves energy and momentum more effectively than simpler methods. The Velocity-Verlet algorithm updates the positions and velocities of particles systematically, ensuring that the simulation remains stable and accurate over long periods. Calculating new positions based on current velocities and forces allows for a more realistic representation of particle dynamics, which is crucial for studying complex systems. The Velocity-Verlet algorithm is represented as follows^{30,31}.

$$r(t + \Delta t) = r(t) + v(t)(\Delta t) + 1/2 \left(\frac{d^2 r}{dt^2} \right) (\Delta t)^2 \quad (\text{a-2})$$

$$v(t + \Delta t) = v(t) + \frac{\Delta t (a(t) + a(t + \Delta t))}{2}. \quad (\text{a-3})$$

Force fields play a vital role in MD simulations by defining the potential energy associated with interactions among particles. These mathematical models describe how particles attracted or repelled each other based on their distances. The choice of force field significantly affected the accuracy of simulation results, as it determined how accurately the model captures the physical reality of system being studied. Understanding the importance of force fields helps researchers select the most appropriate models for their specific applications, leading to more reliable predictions of material behavior. Lennard-Jones (LJ), modified embedded atom model (MEAM) for metal particles, and Coulomb potential functions for charged particles are used^{32–34}. The LJ potential function is represented as follows³⁴.

$$U_{LJ} = 4\varepsilon_{ij} \left[\left(\frac{\sigma_{ij}}{r_{ij}} \right)^{12} - \left(\frac{\sigma_{ij}}{r_{ij}} \right)^6 \right] \quad r < r_c. \quad (\text{a-4})$$

In the above equation, ε_{ij} represents the depth of potential well, σ_{ij} is the distance at which the potential between two particles was zero, and r_{ij} is the distance among particles. LJ Coefficients are calculated using^{35,36} references. EAM potential function is represented in the following³³:

$$U_i = F_\alpha \left(\sum_{j \neq i} \rho_\beta(r_{ij}) \right) + \frac{1}{2} \sum_{j \neq i} \phi_{\alpha\beta}(r_{ij}) \quad (\text{a-5})$$

F_α is a constant value in the range of 0 to 1 within this equation. The density of atomic charges causes ρ_β and $\phi_{\alpha\beta}$ is caused by the presence of particles in the simulation box. The Coulomb force field is represented as follows³⁵.

$$U_{ij}(r) = \frac{-1}{4\pi\varepsilon_0} \frac{q_i q_j}{r_{ij}^2}, \quad (\text{a-6})$$

where, q_i and q_j are the charges of interacting particles, and r_{ij} is the distance among them.

Received: 2 August 2024; Accepted: 13 November 2024

Published online: 16 November 2024

References

1. Panda, P. Environmental friendly lead-free piezoelectric materials. *J. Mater. Sci.* **44**(19), 5049–5062 (2009).
2. Adediji, Y. B., Adeyinka, A. M., Yahya, D. I. & Mbelu, O. V. A review of energy storage applications of lead-free BaTiO₃-based dielectric ceramic capacitors. *Energy Ecol. Environ.* **8**(5), 401–419 (2023).
3. Mariello, M. Advanced lead-free piezoelectric materials: ceramics, polymers, and composites. In *Handbook of Energy Materials* (ed. Gupta, R.) 1–41 (Springer, 2022).
4. Aksel, E. & Jones, J. L. Advances in lead-free piezoelectric materials for sensors and actuators. *Sensors* **10**(3), 1935–1954 (2010).
5. Zhao, C., Huang, Y. & Wu, J. Multifunctional barium titanate ceramics via chemical modification tuning phase structure. *InfoMat* **2**(6), 1163–1190 (2020).

6. Deng, C. et al. Recent progress on barium titanate-based ferroelectrics for sensor applications. *Adv. Sens. Res.*, 2300168 (2024).
7. Ramasubramanian, B. et al. Novel low-carbon energy solutions for powering emerging wearables, smart textiles, and medical devices. *Energy Environ. Sci.* **15**(12), 4928–4981 (2022).
8. Nor, N. M., Hamzah, H. H. & Razak, K. A. Recent advancement in sustainable energy harvesting using piezoelectric materials. In *Sustainable Materials for Next Generation Energy Devices* (eds Nor, N. M. et al.) 221–248 (Elsevier, 2021).
9. Rödel, J. et al. Transferring lead-free piezoelectric ceramics into application. *J. Eur. Ceram. Soc.* **35**(6), 1659–1681 (2015).
10. Shahraiki, M. G., Ghorbanali, S. & Savaloni, H. Influence of crystallographic orientation and diameter on piezoelectric constant and Young's modulus of BaTiO₃ nanobelts. *Solid State Commun.* **196**, 40–45 (2014).
11. Wang, S. et al. A core-shell structured barium titanate nanoparticles for the enhanced piezoelectric performance of wearable nanogenerator. *Appl. Energy* **351**, 121835 (2023).
12. Cai, E., Liu, Q. & Gu, H. Optimization of the electrical properties on lead-free barium titanate-based piezoelectric by combining grain growth with orthorhombic-tetragonal phase boundary. *J. Alloys Compd.* **948**, 169775 (2023).
13. Chen, K., Yang, C. & Tang, B. Study on the phase structure and electrical properties of lead-free Barium titanate-based piezoelectric ceramic. *J. Phys. Conf. Ser.* **2680**, 012008 (2024).
14. Esmaeili, S., Ehsani, M., Toghraie, D. & Saber-Samandari, S. The investigation of piezoelectric features of lead-free barium titanate ceramic materials at different initial Temps in the tetragonal phase using molecular dynamics simulation. *Results Phys.* **63**, 107851 (2024).
15. Kassem, W. *Direct Molecular Dynamics Simulation of Piezoelectric and Piezothermal Couplings in Crystals* (Ecole Centrale Paris, 2015).
16. Vlachakis, D., Bencurova, E., Papangelopoulos, N. & Kossida, S. Current state-of-the-art molecular dynamics methods and applications. *Adv. Protein Chem. Struct. Biol.* **94**, 269–313 (2014).
17. Huggins, D. J. et al. Biomolecular simulations: From dynamics and mechanisms to computational assays of biological activity. *Wiley Interdiscipl. Rev. Comput. Mol. Sci.* **9**(3), e1393 (2019).
18. Hanwell, M. D. et al. Avogadro: an advanced semantic chemical editor, visualization, and analysis platform. *J. Cheminform.* **4**, 1–17 (2012).
19. Lematre, M., Ul, R., Gratton, M., Tran-Huu-Hue, L.-P. & Lethiecq, M. Modeling of the electromechanical behavior of barium titanate under mechanical stress and comparison with experimental measurements. *IEEE Trans. Ultrasonics Ferroelectr. Freq. Control* **67**(8), 1715–1724 (2020).
20. Frenkel, D. & Smit, B. *Understanding Molecular Simulation: from Algorithms to Applications* (Elsevier, 2001).
21. Ngai, K. *Relaxation and Diffusion in Complex Systems* (Springer Science & Business Media, 2011).
22. Nobarani, H. & Zaeem, M. A. A molecular dynamics study of domain switching in BiFeO₃ nanofilm under DC electric field. *Comput. Mater. Sci.* **199**, 110718 (2021).
23. Miller, S., Schwank, J., Nasby, R. & Rodgers, M. Modeling ferroelectric capacitor switching with asymmetric nonperiodic input signals and arbitrary initial conditions. *J. Appl. Phys.* **70**(5), 2849–2860 (1991).
24. Wang, L. et al. Modeling ferroelectric capacitors based on the dipole switching theory. *J. Appl. Phys.* <https://doi.org/10.1063/1.2729470> (2007).
25. https://docs.lammps.org/fix_deform.html.
26. Woo, C. & Zheng, Y. Depolarization in modeling nano-scale ferroelectrics using the Landau free energy functional. *Appl. Phys. A* **91**, 59–63 (2008).
27. Wang, X.-Y., Wang, Y.-L. & Yang, R.-J. Lattice model for strained nanoscale ferroelectric capacitors: Investigation on fundamental size limits in ferroelectricity. *Appl. Phys. Lett.* <https://doi.org/10.1063/1.3243338> (2009).
28. Bernal, J. D. A geometrical approach to the structure of liquids. *Nature* **183**, 141–147 (1959).
29. Rapaport, D. C. & Rapaport, D. C. R. *The Art of Molecular Dynamics Simulation* (Cambridge University Press, 2004).
30. Verlet, L. Computer "experiments" on classical fluids. I. Thermodynamical properties of Lennard-Jones molecules. *Phys. Rev.* **159**(1), 98 (1967).
31. Vetterling, W. T., Teukolsky, S. A., Press, W. H. & Flannery, B. P. *Numerical Recipes in C: The Art of Scientific Computing* (Cambridge University Press, 1999).
32. Daw, M. S. & Baskes, M. I. Embedded-atom method: Derivation and application to impurities, surfaces, and other defects in metals. *Phys. Rev. B* **29**(12), 6443 (1984).
33. Lennard-Jones, J. E. Cohesion. *Proc. Phys. Soc.* **43**(5), 461 (1931).
34. Huray, P. G. *Maxwell's Equations* (Wiley, 2011).
35. Rappé, A. K., Casewit, C. J., Colwell, K., Goddard, W. A. III. & Skiff, W. M. UFF, a full periodic table force field for molecular mechanics and molecular dynamics simulations. *J. Am. Chem. Soc.* **114**(25), 10024–10035 (1992).
36. Mayo, S. L., Olafson, B. D. & Goddard, W. A. DREIDING: a generic force field for molecular simulations. *J. Phys. Chem.* **94**(26), 8897–8909 (1990).

Author contributions

B and C. Conceived of the presented idea. A. Developed the theory and performed the computations. B, C, and D. Verified the analytical methods and supervised the findings of this work. All authors discussed the results and contributed to the final manuscript.

Declarations

Competing interests

The authors declare no competing interests.

Additional information

Correspondence and requests for materials should be addressed to M.H.E.

Reprints and permissions information is available at www.nature.com/reprints.

Publisher's note Springer Nature remains neutral with regard to jurisdictional claims in published maps and institutional affiliations.

Open Access This article is licensed under a Creative Commons Attribution-NonCommercial-NoDerivatives 4.0 International License, which permits any non-commercial use, sharing, distribution and reproduction in any medium or format, as long as you give appropriate credit to the original author(s) and the source, provide a link to the Creative Commons licence, and indicate if you modified the licensed material. You do not have permission under this licence to share adapted material derived from this article or parts of it. The images or other third party material in this article are included in the article's Creative Commons licence, unless indicated otherwise in a credit line to the material. If material is not included in the article's Creative Commons licence and your intended use is not permitted by statutory regulation or exceeds the permitted use, you will need to obtain permission directly from the copyright holder. To view a copy of this licence, visit <http://creativecommons.org/licenses/by-nc-nd/4.0/>.

© The Author(s) 2024